PROCEEDINGS A

royalsocietypublishing.org/journal/rspa

Research

Cite this article: Jain U. 2026 Bond front velocity in lubrication-mediated bonding of flexible substrates. *Proc. R. Soc. A* **482**: 20260071.
https://doi.org/10.1098/rspa.2026.0071

Received: 22 January 2026
Accepted: 26 March 2026

Subject Areas:
mechanics, fluid mechanics, nanotechnology

Keywords:
wafer bonding, semiconductor assembly, 3D integration

Author for correspondence:
Utkarsh Jain
e-mail: utkarsh.jain@imec.be

Electronic supplementary material is available online at https://doi.org/10.6084/m9.figshare.c.8452075.

THE ROYAL SOCIETY PUBLISHING

Bond front velocity in lubrication-mediated bonding of flexible substrates

Utkarsh Jain

imec, Leuven 3001, Belgium

UJ, 0000-0002-1014-7861

Bonding and assembly processes have started to take the centre-stage in semiconductor manufacturing as they enable three-dimensional (3D) stacking and heterogeneous integration for novel interconnect architectures of integrated circuits. The progression of a bond front hinges on balance of adhesion and dissipation forces. Here, a lubrication–elasticity model is reported, to elucidate near-field dynamics of the process while staying within continuum limits, excluding adhesion mechanisms. When governed by lubrication flow in the gap, and linear elasticity in the substrates, the unbonded part of the substrates assumes a power-law shape as a function of the distance from the bond front. Furthermore, an entirely self-consistent formulation for the bond front velocity is derived. The formulation presented here crucially relies on a re-parameterization of the problem in terms of a 'high viscous dissipation region' ahead of the bond front, which travels along with the adhesion front. This approach for expressing the bond front velocity allows for its acceleration as the unbonded region shrinks, for example with bond front approaching the edge of a finite substrate. Finally, unifying velocity and length scales are proposed, incorporating a lateral adhesion front length scale that effectively captures velocity variations in the limit of vanishing viscous dissipation, bridging continuum and molecular scales. This framework provides scalable insights for better understanding and process control in applications with wafer and die bonding.

1. Introduction

Wafer and die bonding are pivotal technologies in semiconductor manufacturing, enabling the integration of diverse materials and structures to meet the demands

of advanced microelectronics, microelectromechanical systems and three-dimensional (3D) integrated circuits [1,2].

The bonding process involves the adhesion of two substrates, where a bond front propagates laterally, driven by work of adhesion and opposed by dissipative mechanisms chiefly in the intervening gas layer. This process facilitates the permanent or temporary joining of substrates, supporting applications such as silicon-on-insulator substrates [3], backside-illuminated complementary metal-oxide-semiconductor image sensors [4,5] and high-density 3D stacking for memory-on-logic architectures [6]. Commercial bonding systems from tool vendors achieve remarkable alignment accuracy, with sub-micron overlay precision for 300 mm wafer-to-wafer bonding [7–10]. However, the fundamental mechanisms governing bond front propagation—particularly the interplay of surface adhesion, viscous dissipation and substrate deformation, remain under-explored. This limits process optimization and scaling for next-generation devices, and limits the understanding of further undesired mechanical effects owing to unsteady bond front progression (such as its complete halt or acceleration near the edge of a finite substrate).

The scientific foundation of wafer bonding traces back to early studies of adhesion and fracture, such as Obreimoff's work on cleavage [11] and Rayleigh's study of glass surfaces brought into contact [12]. Since these early works, key principles of adhesion fronts and related bonding dynamics have been established in works by Yu & Sou [13] by explaining criteria for bonding in terms of elastic accommodation, by Turner *et al.* [14,15] by explaining the bondability of substrates based on balance adhesion and strain energy, by Bengtsson [16] experimentally showing bond front speeds with substrates of different dimensions, and by Gösele *et al.* [17,18] by performing bonding in different ambient conditions. Continuum-scale bond front dynamics in terms of linear elasticity and lubrication flows have also been analytically and experimentally explored by Rieutord *et al.* [19], Navarro *et al.* [20,21], Radisson *et al.* [22,23]. Other means of dissipation in the gas have also been suggested, such as molecular motion by Liao *et al.* [24] and molecular–viscous dissipation by Bengtsson *et al.* [16]. More recently, Poulain *et al.* [25] and Carlson *et al.* [26] also advanced the elastohydrodynamic framework for bonding, particularly applicable for bonding of thin substrates such that van der Waals' and Lennard-Jones mechanisms become relevant alongside lubrication stresses in the regime of small gap widths.

In this paper, we build on the insights of the above mentioned literature and bring our attention on continuum description of bonding dynamics. We omit near-field adhesion front dynamics occurring at sub-continuum gap heights, which would manifest in lubrication equations as conjoining/disjoining type of pressures. Quantitative arguments are given supporting the omission. In §2, we present a lubrication–elasticity framework for axisymmetric bonding dynamics, coupling thin-plate bending theory with lubrication flow to first derive a power-law solution (§2c) for the substrate shape that it would assume while bonding in a free-hanging state. We find the same power-law result for the shape of the unbonded span of the wafers (also, the gap shape) as found by Rieutord *et al.* [19] and Liao *et al.* [24] by balancing lubrication pressure gradient with linear elasticity in planar coordinates. We also show the pre-factors to the power law can be entirely self-consistently derived from the governing equations (§2c(ii)).

Next in §3, using the same energy balance arguments from work of adhesion and dissipation in intervening gas as Bengtsson [16], Rieutord *et al.* [19] and Poulain *et al.* [25], we derive an expression for the bond front velocity. We find an intermediate integral formulation of the same form as [19] for the front velocity, which is initially suggestive of the same power-law dependencies on material properties (substrate thickness, Young's modulus, gas viscosity) and surface energy as those suggested by Bengtsson *et al.* [16]. The above-mentioned integral formulation for bond front velocity runs along the coordinate of the bond front's progression. We show that this intermediate formulation cannot yield meaningful values for the bond front velocity, as it diverges with distance. This issue occurs naturally in the formulation, and surprisingly has not been addressed before. Here, we deviate from the above mentioned works [16,19,24,25] by defining the viscous dissipation region in the gas such that its lateral span ought

not extend to infinity (§3c–e). We resolve the issue of the diverging expression by introducing a length scale δ concerning a 'high dissipation region', wherein much of the viscous dissipation ahead of the bond front is concentrated. This dissipation volume travels ahead of the bond front. Dissipation profiles in the gas are computed which justify the use of such a length scale to re-parameterize the expression for bond front velocity. This approach provides meaningful values for bond front velocity, in close agreement with usually reported values in experiments [16,19,27]. The re-parameterized formulation for the front velocity is shown to be highly versatile. This approach can intrinsically account for shrinking of this high-dissipation region in the gas (§4a), which results in the acceleration of the bond front as it approaches the edge of a finite substrate (also an effect observed in experiments [19,21]). We show that the increase in bond front velocity near the edge also makes the substrate shape steeper, with undesired consequences for post-bonding defects (creating localized in-plane stretches, or causing condensation voids owing to isenthalpic gas expansion, or Joule–Thomson condensation [28, p. 236]).

Finally in §4b, we discuss the velocity and length scales that ought to characterize the bond front velocity both in the steady-state (far-from-edge) regime, and its steep increase close to the edge of a finite substrate. In the former case, the velocity scale can be inferred from the steady-state derivation, while a trivial length scale of the substrate size is sufficient to describe the dynamics. However, when the front accelerates on account of the shrinking dissipation region ahead of the bond front, the substrate size is not a representative length scale. Close to the substrate edge, the closing gap pushes the continuum framework to the limits of its applicability, and we introduce a natural length scale to characterize the lateral extent of the adhesion front, inspired by a similar length scale introduced by Poulain *et al.* [25] in the Lennard-Jones repulsion-limited bonding dynamics. This length scale completely collapses the acceleration profiles of the bond front close to the edge. We first start with setting up the problem in §2.

2. Dimensional governing equations

We consider two circular plates in axisymmetric coordinates with r being the radial coordinate and z being the vertical coordinate across the gap. The gap height is $2h(r,t)$, with the bottom wafer at $z=-h(r,t)$ and the top wafer at $z=h(r,t)$, symmetric about $z=0$. The bond front propagates radially at $r=r_f(t)$ with velocity $U=\mathrm{d}r_f/\mathrm{d}t$. The pressure $P(r,t)$ within the gap drives air escape, with ambient pressure $P(r\to\infty,t)=P_0$. A schematic is shown in figure 1.

The radial velocity $v_r(z,r,t)$ of air in the gap is governed by the Navier–Stokes equations under the lubrication approximation ($2h\ll r$) [29],

$$\eta\frac{\partial^2 v_r}{\partial z^2}=\frac{\partial P}{\partial r}, \tag{2.1}$$

where η is the air viscosity, where the usual approximations hold, namely that of no vertical pressure gradient: $\partial^2 v_r/\partial r^2 \ll \partial^2 v_r/\partial z^2$, and no-slip boundary conditions apply at the inner surfaces of the substrates: $v_r=0$ at $z=\pm h(r,t)$. In both gas- and liquid-mediated bonding processes, the lubrication approximation in equation (2.1) remains valid as long as the gap height $2h$ is much larger than the mean free path Λ of the fluid (e.g. approx. 68 nm for air at atmospheric pressure [30]).

For liquid-mediated bonding, the region of applicability of lubrication equation holds down to the roughness scale of the substrates (often in angstroms [31,32]), where short-ranged adhesion mechanisms (such as van der Waals' forces) will noticeably contribute to the force balance between the substrates' elastic rigidity and the driving pressure pulling them towards each other. This effect will manifest as conjoining pressure, applicable at a gap widths determined by van der Waals' forces with a Hamaker constant dependent on the adhering surfaces [33]. The treatment in this manuscript does not treat this effect explicitly, and a quantitative justification for this is given in §2b.

In a gas-mediated bonding process, lubrication assumptions remain valid provided we consider length scales greater than the mean free path. At these length scales, lubrication theory

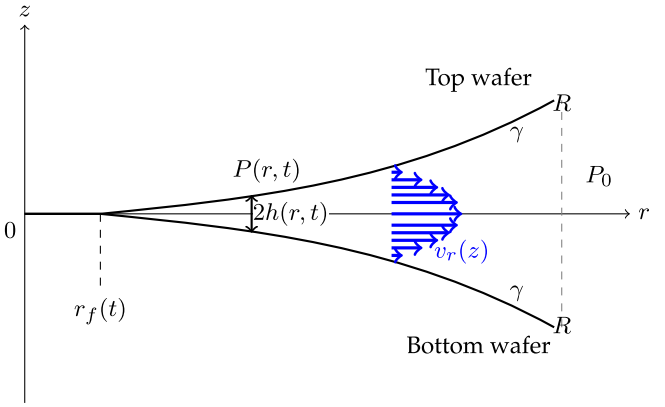

Figure 1. Axisymmetric wafer bonding geometry for substrates of radius R (highlighted as distance from $r = 0$ by the grey-dashed line). The gap height $2h(r, t)$ separates the wafers, with the bond front at $r = r_f(t)$. Lubrication pressure gradient in the gap drives the substrates towards each other, with $P(r, t)$ being an effective loading, balanced by the bending rigidity of the substrates. Beyond the edges of the substrates, ambient conditions can exist at some pressure P_0. Blue arrows indicate the quadratic flow profile that develops in the gap with no-slip boundary conditions imposed at the solids. The two substrates release energy upon bonding, the adhesion surface energy per unit area on the unbonded surfaces, γ, is shown on both (assumed equal for both the surfaces).

still remains unaffected by van der Waals forces. At even smaller gap widths, the adhesion front could be strongly influenced by van der Waals' or hydrogen bonds depending on the charged species or dangling bonds present on the bonding surfaces [34], while free molecular flow description would hold for the gas flow in gaps $2h \lesssim \mathcal{O}(\sim \Lambda)$. The quantitative justification for excluding the conjoining pressure in this medium is also given in §2b.

(a) Driving pressure gradient

Integrating equation (2.1) with the above mentioned boundary conditions yields the well-known Poiseuille flow,

$$v_r(z) = \frac{1}{2\eta}\frac{\partial P}{\partial r}(z^2 - h^2), \tag{2.2}$$

which yields a volumetric flow rate of

$$Q(r, t) = 2\pi r \int_{-h}^{h} v_r(z)\,\mathrm{d}z = 2\pi r \cdot \frac{1}{\eta}\frac{\partial P}{\partial r}\int_0^h (z^2 - h^2)\,\mathrm{d}z = -\frac{4\pi r h^3}{3\eta}\frac{\partial P}{\partial r}. \tag{2.3}$$

This can be related to the dynamics of the substrate shape $h(t)$, as $Q(r, t)$ is directly influenced by the gap closure,

$$\frac{\partial(2h)}{\partial t} + \frac{1}{r}\frac{\partial(rQ)}{\partial r} = 0, \tag{2.4}$$

which can be rearranged to yield

$$\frac{\partial h}{\partial t} = \frac{2\pi}{3\eta r}\frac{\partial}{\partial r}\left(rh^3\frac{\partial P}{\partial r}\right). \tag{2.5}$$

Note that the time derivative gives a dynamical description of h, but the description of air flow remains quasi-static from equation (2.2). Since Q at at $r = r_f$ should match the rate of volume of

https://royalsocietypublishing.org/journal/rspa Proc. R. Soc. A 482: 20260071

fluid displaced, a definition for depth-averaged fluid velocity U_d can be written as

$$U_d = \frac{Q(r,t)}{2\pi r \cdot 2h(r,t)}, \tag{2.6}$$

and equation (2.3) can be used to rewrite the pressure gradient as

$$\frac{\partial P}{\partial r} = -\frac{3\eta U_d(r,t)}{h(r,t)^2}, \tag{2.7}$$

similar to the expression derived by [19] in two dimensions following similar physical considerations.

(b) Governing equation coupling the lubrication pressure to wafer deformation

As the bond front progresses, squeezing out the fluid in the gap, each wafer deflects by $h(r,t)$ with bending stresses being balanced by the lubrication pressure gradient. Using thin-plate bending theory:

$$D\nabla^4 h = P(r,t) - P_0 \quad \text{and} \quad D = \frac{ET^3}{12(1-\nu^2)}, \tag{2.8}$$

where E is the elastic modulus of the substrate, T the thickness, ν Poisson's ratio, D is the bending rigidity [35, p. 42] and P_0 is the ambient pressure at the edges of the substrates. The biharmonic operator [36, p. 143] in axisymmetric coordinates is used:

$$\nabla^4 h = \frac{\partial^4 h}{\partial r^4} + \frac{2}{r}\frac{\partial^3 h}{\partial r^3} - \frac{1}{r^2}\frac{\partial^2 h}{\partial r^2} + \frac{1}{r^3}\frac{\partial h}{\partial r}, \tag{2.9}$$

while an equivalent expression for $P(r,t) - P_0$, which acts as the loading in equation (2.8), has already been derived in equation (2.7). Equation (2.7) takes the following form upon integration:

$$P(r,t) - P_0 = -\int_{r \to r_f}^{r} \frac{3\eta U_d(r',t)}{h(r',t)^2}\, \mathrm{d}r', \tag{2.10}$$

with an indeterminate upper limit. In the limit $r \to r_f$, we may define bond front velocity $U \approx \mathrm{d}r_f/\mathrm{d}t$. Near the bond front, we approximate $U_d(r,t) \approx U$, as the flow is dominated by the front's motion and the gap height changes slowly.

For small gaps where van der Waals' or similar types of attractive forces become non-negligible, the system shown in equation (2.8) could be augmented by adding a conjoining pressure term as an additional loading term. The lubrication pressure gradient that is driving the flow can depend on the velocity U_d, and thus on Q and h. However, assuming a steady-state bond front progression (implying constant U), and with the approximation of $U_d \approx U$, the pressure difference scales as h^{-2} following equation (2.10). In contrast, the *velocity-independent* conjoining pressure from the van der Waals interactions scales as approximately $H_A/(6\pi h^3)$ [37, p. 267], where H_A is the Hamaker constant for a given pair of surfaces. With these conditions, near the bond front, the viscous term grows as $1/h^2$ while the conjoining term grows faster ($1/h^3$), potentially becoming dominant at sufficiently small h.

This conjoining pressure, arising from van der Waals' or other interactions, can dominate the plate's deflection in the immediate vicinity of the bond front ($r \approx r_f$). The region where it might compete with lubrication pressure is thus estimated. First, we use equation (2.10) to identify the characteristic pressure differential in the lubrication domain as $\Delta P \sim 3\eta UR/h_{\text{far-field}}^2$, where we have made use of the approximation $U_d \approx U$. The lateral characteristic length scale in ΔP is taken to be the unbonded region (spanning upto the wafer radius R), and the far-field value of the unbonded gap width $h_{\text{far-field}}$ as the vertical length scale. Using the dynamic viscosity of air 1.8×10^{-5} Pa s, $U = 3$ cm s^{-1} (from experimental literature [19,20,27]), $R = 150$ mm, $h_{\text{far-field}} \sim 10\,\mu$m and $\Delta P \approx 2.45 \times 10^3$ Pa. Thus, the determined ΔP can be equated with the van der Waals pressure to find the approximate gap width h_{conj} below which, van der Waals' adhesion acting as conjoining pressure, may start competing with lubrication pressure to affect the bending.

From such a balance, the vertical gap height $h_{\text{conj}} \approx (H_A/6\pi\,\Delta P)^{1/3}$. Using $H_A = 5.4 \times 10^{-20}$ J (from [33]), $h_{\text{conj}} \approx 11$ nm. At such a gap width h_{conj}, the lateral length span of influence of conjoining pressure l_{conj}, can be estimated by considering the bending resistance from equation (2.8), while using the mechanical properties of a silicon wafer as $E = 130$ GPa, $T = 775\,\mu$m and $\nu = 0.28$, yielding $D \approx 5.47$ N m. Equation (2.8) suggests balancing the pressure scale with the van der Waals pressure as $Dh_{\text{conj}}/(2l_{\text{conj}})^4 \sim H_A/6\pi h_{\text{conj}}^3$. This balance yields $l_{\text{conj}} \approx 1.1$ mm, ahead of the bond front.

Similar comments may be made for bonding in the presence of moisture in the ambient surroundings, or on the bonding surfaces. For instance, water monolayers on the bonding surfaces [34] may spontaneously clump to form capillary bridges when the gap size approaches a critical bonding-gap (called the Kelvin length [38]). With the presence of water either in the form of capillary bridges, or as a uniform interlayer at the bonding surface, the continuum approximation may only break down at length scales approaching the surface roughness of the substrates ($\mathcal{O} \sim$ Å). The effective H_A in this region will take a different (smaller) value owing to the presence of liquid medium, with the conjoining pressure's region of influence analogous to l_{conj} determined above. Such a lateral span of influence, using a gap height $h_{\text{Å}}$ originating from roughness of the surfaces undergoing bonding, and flexural rigidity $D \approx 5.47$ N m, can be determined by balancing the van der Waals force with bending stress as $H_A/6\pi h_{\text{Å}}^3 \sim Dh_{\text{Å}}/(2l_{\text{liq, conj}})^4$, where $H_A \approx 10^{-21}$ J [39] for angstrom-level roughness of two surfaces. Using $h_{\text{Å}} \sim 0.3$ nm, $l_{\text{liq, conj}} \approx 85\,\mu$m from the bond front. Since $l_{\text{conj}} \ll R$ in both cases, and both elasticity and viscous dissipation generally act over the scale of the substrate size, we neglect the conjoining pressure term's contributions, and focus on the lubrication–elasticity framework governing the far-field dynamics. The approximations for l_{conj} indicate the limits of the model's applicability near the bond front, but allow a tractable analysis of the bond front propagation driven by lubrication pressure and substrate bending.[1]

(c) Solution to the governing equation

A solution is sought to the governing equation (2.8). Carlson *et al.* [25,26] solved a similar bonding problem of a thin film, in the framework of elastohydrodynamics, deriving a travelling-wave solution for the 'peeling' front which a moving liquid-filled blister travels with in its windward direction [25], and similarity solutions for the bonding or 'adhesion' front [26] which happen to be on the leeward side of the liquid-filled blister. However, our integro-differential governing equation has the same form as the governing equation derived by Rieutord *et al.* [19] in planar coordinates, for wafers bonding owing to the lubrication–plane-strain coupling, albeit with the additional terms owing to axisymmetric biharmonic operator. Rieutord *et al.* [19] non-dimensionalized the system using a length scale $l = \sqrt{D/3\eta U}$ before showing that a power-law ansatz for the wafer shape in the scaled coordinates satisfies the governing equation. Here, we show that this intermediate step of non-dimensionalizing the system is not strictly required, and the power-law ansatz can be directly applied to the dimensional governing equation, but with limitations owing to the axisymmetric coordinates.

The biharmonic operator in equation (2.8) is in axisymmetric coordinates. Owing to the linearity of the operator ∇^4, the solution can be expressed as a sum of a particular solution $h_p(r,t)$ which accounts for the lubrication-driven pressure, and a homogeneous solution $h_h(r,t)$, which satisfies $\nabla^4 h_h = 0$. The latter may take a form

$$h_h(r,t) = c_1(t) + c_2(t)r^2 + c_3(t)\ln r + c_4(t)r^2 \ln r, \tag{2.11}$$

[1]Note that such estimations of ΔP above assume $U_d \approx U$ over the entire unbonded region of size R. However, away from the bond front where adhesion effects are negligible, equation (2.8) requires a balance between the bending term (approx. Dh/R^4) and the fluid pressure term (approx. $\eta U_d R/h^2$), which can only be satisfied if $U_d \ll U$ over much of the unbonded region. This implies ΔP is probably an overestimate, and consequently h_{conj} and l_{conj} may be underestimated. This issue is left unresolved, since these quantities do not enter the subsequent analysis, and the main results discussed henceforth in the paper are unaffected.

where the terms in $h_h(r,t)$ (the constants $c_{1,2,3,4}$) could help capture the full shape of the substrate far from the bond front with typical boundary conditions (free, rotation-only or clamped) imposed.

Note that in terms of energy balance, the bond front's propagation is favoured by high adhesion energy of the surfaces, and opposed by viscous dissipation in the gap. Viscous flows in corner geometries tend to have high dissipation approaching singularities in the corner [40]. This implies that dissipation far from the bond front has a weakening influence on determining the bond front's dynamics, and for simplicity in obtaining h_p, a Cartesian approximation may suffice near the bond front. From experimental observations by Rieutord *et al.* [19] and modelling of Radisson [22] (albeit both for one-dimensional bond front propagation), we can ignore h_h, and use a monotonic shape for the solution $h_p(r,t)$ to the integro-differential equation (2.8).

Thus, for h_p where a bonding surface is shaped by the governing equation in equation (2.8), we seek a power-law solution for the unbonded gap, with its opening angle pointing towards the direction of bond front propagation, and its origin pinned to the moving bond front's location (in this case, $r = r_f$).

(i) Power-law ansatz

Since h_h is ignored, for simplicity we change the notation from h_p to h, and in the vicinity of the bond front, and propose the power-law ansatz

$$h(r,t) = A(r - r_f)^{\alpha}, \tag{2.12}$$

where A is initially introduced as a proportionality constant with dimensions of $[L]^{1-\alpha}$. Applying the biharmonic operator to equation (2.12),

$$\frac{\partial h}{\partial r} = \alpha A(r - r_f)^{\alpha-1}, \quad \frac{\partial^2 h}{\partial r^2} = \alpha(\alpha-1)A(r - r_f)^{\alpha-2},$$

$$\frac{\partial^3 h}{\partial r^3} = \alpha(\alpha-1)(\alpha-2)A(r - r_f)^{\alpha-3}, \quad \frac{\partial^4 h}{\partial r^4} = \alpha(\alpha-1)(\alpha-2)(\alpha-3)A(r - r_f)^{\alpha-4}$$

and

$$\nabla^4 h = A(r - r_f)^{\alpha-4}\left[\alpha(\alpha-1)(\alpha-2)(\alpha-3) + \frac{2\alpha(\alpha-1)(\alpha-2)(r - r_f)}{r} - \frac{\alpha(\alpha-1)(r - r_f)^2}{r^2} + \frac{\alpha(r - r_f)^3}{r^3}\right].$$

Near $r \approx r_f$, $r - r_f \ll r_f$, and $r \approx r_f$ where viscous dissipation is concentrated, the dominant term is

$$\nabla^4 h \approx A\alpha(\alpha-1)(\alpha-2)(\alpha-3)(r - r_f)^{\alpha-4}. \tag{2.13}$$

This can be equated to the powers of r in equation (2.10):

$$P(r,t) - P_0 = \frac{3\eta U}{A^2(2\alpha-1)}(r - r_f)^{1-2\alpha}. \tag{2.14}$$

Balancing the exponents in equations (2.14) and (2.13) yields $\alpha = 5/3$. Thus in the region where the stress balances, lubrication–elasticity dominates over molecular interactions (adhesive/repulsive potentials [25,41]), and we get the final expression for substrate/gap shape as

$$h(r,t) = A(r - r_f)^{5/3}. \tag{2.15}$$

This is the same exponent as found by Rieutord *et al.* [19], but the definition and meaning of parameter A is different. While in [19] the governing equation was rescaled by length scale $l \equiv \sqrt{\frac{D}{3\eta U}}$ (determined therein to be approx. 3000 m) and A was determined to be a constant (approx. 0.95), in the present paper we do not introduce l owing to its magnitude being fairly unrepresentative of the problem (with standard wafers usually being 300 mm in diameter and thickness (approx. 800 µm). Instead, the dimensional parameters present in l in [19] are absorbed in the now dimensional, parameter A.

(ii) Determining the parameter A

Parameter A can be estimated from the existing expressions by equating the pressure balances: $P(r,t)-P_0$ from the flow description, with the pressure balance from $D\nabla^4 h$.

Lubrication term: With $h(r,t)=A(r-r_f)^{5/3}$ known, the pressure differential in the flow can be obtained from equation (2.10) as

$$P(r,t)-P_0=-\int_{r_f}^{r}\frac{3\eta U}{A^2(r'-r_f)^{10/3}}\,\mathrm{d}r', \tag{2.16}$$

with boundary condition $P(r\to\infty,t)=P_0$. Let $u=r'-r_f$, so $\mathrm{d}r'=\mathrm{d}u$, and limits change from $r'=r_f$ to $r'=r$, or $u=0$ to $u=r-r_f$,

$$P(r,t)-P_0=-\frac{3\eta U}{A^2}\int_0^{r-r_f}u^{-10/3}\,\mathrm{d}u.$$

The integral is computed as $-\frac{3}{7}u^{-7/3}$ and evaluated with the limits

$$\left[-\frac{3}{7}u^{-7/3}\right]_0^{r-r_f}=-\frac{3}{7}(r-r_f)^{-7/3}-\lim_{u\to 0^+}\left(-\frac{3}{7}u^{-7/3}\right).$$

The limit at $u\to 0^+$ at the bond front diverges, but this is expected and we may ignore the term as the continuum approximation should cease to hold as $h\to 0$. The first term remains finite,

$$P(r,t)-P_0=-\frac{3\eta U}{A^2}\cdot\left(-\frac{3}{7}(r-r_f)^{-7/3}\right)=\frac{9\eta U}{7A^2}(r-r_f)^{-7/3}. \tag{2.17}$$

Bending term: Equation (2.13) with $\alpha=5/3$ yields

$$\nabla^4 h=A\cdot\frac{40}{81}(r-r_f)^{-7/3}. \tag{2.18}$$

Finally equating equation (2.17) with equation (2.18), the $(r-r_f)^{-7/3}$ terms cancel,

$$\frac{9\eta U}{7A^2}=\frac{40DA}{81},$$

which is rearranged to get $A=\left(\frac{729\eta U}{280D}\right)^{1/3}$. Writing out material constants in D explicitly,

$$A=\left(\frac{2187\eta U(1-\nu^2)}{70ET^3}\right)^{1/3}. \tag{2.19}$$

Note that the dependence of A on U implies a dependence of $h(r,t)$ equation (2.15) on U. This implies that a rising bond front velocity can inherently affect the shape, in particular where parameter A then determines the local steepness of the substrate shape near the bond front.

3. Mechanisms determining bond front velocity

The bond front velocity (U) is determined by balancing the rate of energy release driving the bonding process against the rate of energy dissipation in the system. Three components in the former can be the rate of release of surface energy ($\dot{E}_{\mathrm{surf}}$ owing to work of adhesion), and the rate of energy gained by unbending the wafers ($\dot{E}_{\mathrm{unbend}}$). While the dominant dissipative mechanism is the viscous dissipation in the lubrication layer ($\dot{E}_{\mathrm{diss}}$).

The rate of surface energy released (for surfaces each with surface energy per unit area γ) can be expressed as

$$\dot{E}_{\mathrm{surf}}=2\pi r_f\gamma U, \tag{3.1}$$

which can be estimated using typical r, $\gamma=0.1\,\mathrm{J\ m^{-2}}$, and reported U [19,27] as approximately 10^{-3} W. The (un)bending energy per unit area can be written as $\mathcal{E}_{\mathrm{unbend}}=\frac{D}{2}(\nabla^2 h)^2$, where D and h are known from equations (2.8) and (2.15). Using the mechanical properties of a Si

https://royalsocietypublishing.org/journal/rspa Proc. R. Soc. A 482: 20260071

(100) crystal with $E = 130\,\text{GPa}$, $T = 775\,\mu\text{m}$, $\nu = 0.28$, it can be determined at some location halfway through a 300 mm wide wafer at $r_f \sim 7.5\,\text{cm}$, to obtain $\mathcal{E}_{\text{unbend}} \approx 0.0008\,\text{J m}^{-2}$, which is approximately two orders of magnitude smaller than γ. Further, an estimate of $\dot{E}_{\text{unbend}}$ can be made as $2\pi r_f U \mathcal{E}_{\text{unbend}} \sim 10^{-5}$ W. Both $\mathcal{E}_{\text{unbend}}$ and $\dot{E}_{\text{unbend}}$ being significantly lower than γ and $\dot{E}_{\text{surf}}$, we try to obtain the final expression for U by balancing $\dot{E}_{\text{surf}}$ soley with the rate of viscous dissipation $\dot{E}_{\text{diss}}$. The functional form of $\dot{E}_{\text{diss}}$ is determined from Poiseuille flow in the gap, in the following subsection.

(a) Viscous dissipation rate

The dissipation rate per unit volume is $\eta(\partial v_r/\partial z)^2$, where $v_r(z, r, t)$ is known from equation (2.2). The viscous dissipation power is calculated over the gap from $z = -h(r, t)$ to $z = h(r, t)$, and radial limits r_{lower} and r_{upper}. These radial limits will be clarified later in §3c once a functional form for U has been derived.

From equation (2.2), the flow velocity gradient is

$$\frac{\partial v_r}{\partial z} = \frac{1}{2\eta}\frac{\partial P}{\partial r}\cdot 2z = \frac{z}{\eta}\frac{\partial P}{\partial r}, \tag{3.2}$$

which is used to define

$$\dot{E}_{\text{diss}} = 2\pi \int_{r_{\text{lower}}}^{r_{\text{upper}}} \int_{-h}^{h} \eta \left(\frac{\partial v_r}{\partial z}\right)^2 r\,\text{d}z\,\text{d}r, \tag{3.3}$$

where equation (3.2) is substituted. Integrating along z, we obtain

$$\dot{E}_{\text{diss}} = \frac{4\pi}{3\eta}\int_{r_{\text{lower}}}^{r_{\text{upper}}} rh^3 \left(\frac{\partial P}{\partial r}\right)^2 \text{d}r. \tag{3.4}$$

The term $\partial P/\partial r$ can be substituted from equation (2.7) and h from equation (2.15), the integrand in equation (3.4) evaluates to

$$rh^3\left(\frac{\partial P}{\partial r}\right)^2 = r\cdot A^3(r-r_f)^5\cdot\frac{9\eta^2U^2}{A^4(r-r_f)^{20/3}} = \frac{9\eta^2U^2r}{A(r-r_f)^{5/3}}. \tag{3.5}$$

This leads us to the final form for viscous dissipation power:

$$\dot{E}_{\text{diss}} = \frac{4\pi}{3\eta}\int_{r_{\text{lower}}}^{r_{\text{upper}}}\frac{9\eta^2U^2r}{A(r-r_f)^{5/3}}\,\text{d}r = \frac{12\pi\eta U^2}{A}\int_{r_{\text{lower}}}^{r_{\text{upper}}}\frac{r}{(r-r_f)^{5/3}}\,\text{d}r. \tag{3.6}$$

(b) Power balance between dissipation and adhesion

The dissipation rates $\dot{E}_{\text{surf}}$ and $\dot{E}_{\text{diss}}$ are balanced as

$$2\pi r_f\gamma U = \frac{12\pi\eta U^2}{A}\int_{r_{\text{lower}}}^{r_{\text{upper}}}\frac{r}{(r-r_f)^{5/3}}\,\text{d}r, \tag{3.7}$$

which can be rearranged to obtain the functional definition of bond front velocity,

$$U = \frac{r_f\gamma A}{6\eta\int_{r_{\text{lower}}}^{r_{\text{upper}}}\frac{r}{(r-r_f)^{5/3}}\,\text{d}r}. \tag{3.8}$$

Here, we would like to highlight the parametric dependencies of U as in equation (3.8),

$$U \propto \gamma A\eta^{-1}, \quad \text{while from equation (2.19): } A \propto \eta^{1/3}U^{1/3}E^{-1/3}T^{-1},$$

which can be rearranged to get

$$U \propto \frac{\gamma^{3/2}}{\eta^1E^{1/2}T^{3/2}}. \tag{3.9}$$

These same parameter dependencies of $E^{-1/2}T^{-3/2}$ were also proposed by Bengtsson *et al.* [16] based on balancing surface energy with sum of the wafer's elastic potential energy and the

https://royalsocietypublishing.org/journal/rspa Proc. R. Soc. A 482: 20260071

gas's kinetic (hence, molecular and not viscous) energy. Naturally since [16] did not consider viscous dissipation in the gas, the bond front velocity proposed therein had no dependence on η. However, we show further that the solution for U in equation (3.9) and more crucially, its parametric dependencies, are incomplete without carefully examining the integral limits in equation (3.8).

(c) The radial limits of the high viscous dissipation zone

(i) Lower limit

As briefly alluded to in §2 and §2c, the lower limit of the integral may be assigned as $r_f + \epsilon$, where ϵ is a short horizontal distance ahead r_f, such that in the region $[r_f, r_f{+}\epsilon)$, continuum (and hence lubrication) approximation for the fluid does not hold. The gap truly closes to zero at r_f, and the substrate's distance h at this location is $h(r_f + \epsilon) = A(\epsilon)^{5/3}$. For bonding in ambient conditions, the fluid could be air, such that $2h = 68\,\text{nm}$.

(ii) Upper limit

Using an upper limit of $r_{\text{upper}} = \infty$ in the integral in equation (3.8) results in $U \to \infty$ with r. Moreover, infinite dissipation over an unbounded domain contradicts the finite energy release rate, rendering $r_{\text{upper}} = \infty$ non-physical. Similarly, using an upper limit of $r_{\text{upper}} = R$ for the radius of a substrate of finite size does not resolve the contradiction arising from $r_{\text{upper}} = \infty$ near $r = r_f$, since the distribution of viscous dissipation near the bond front must be similar regardless of the size of the domain. Since viscous dissipation in this framework is the only way the system spends energy for the bond front to progress, we instead use a different approach to treating its influence, namely by deriving the *cumulative viscous dissipation* distributed along r between $r_f + \epsilon$ and an indeterminate $r_{\text{upper}} = r_f + \delta$.

(d) Cumulative viscous dissipation in the unbonded region

The power of viscous dissipation is given by equation (3.6) with specified limits:

$$\dot{E}_{\text{diss}} = \frac{12\pi\eta U^2}{A} \int_{r_f+\epsilon}^{r_f+\delta} \frac{r}{(r - r_f)^{5/3}}\,\mathrm{d}r. \tag{3.10}$$

Substituting $u = r - r_f$, so $r = u + r_f$, $\mathrm{d}r = \mathrm{d}u$, the integral becomes

$$I = \int_{\epsilon}^{\delta} \frac{u + r_f}{u^{5/3}}\,\mathrm{d}u = r_f \int_{\epsilon}^{\delta} u^{-5/3}\,\mathrm{d}u + \int_{\epsilon}^{\delta} u^{-2/3}\,\mathrm{d}u. \tag{3.11}$$

For a bond initiated at $r = 0$, the bonded region extends over a few millimetres [42–45], after which surface adhesion drives the bond front. For most of the bonding process, $\epsilon, \delta \ll r_f$, where $r_f \sim 10\,\text{mm}$ to $150\,\text{mm}$. This scale separation allows us to introduce a stretched coordinate $\xi = u/\epsilon = (r - r_f)/\epsilon$, with $\mathrm{d}u = \epsilon\,\mathrm{d}\xi$, and limits from $\xi = 1$ (at $u = \epsilon$) to $\xi = \delta/\epsilon$, the integrand becomes

$$\frac{u + r_f}{u^{5/3}} = \frac{\epsilon\xi + r_f}{(\epsilon\xi)^{5/3}} = \epsilon^{-2/3}\xi^{-2/3} + \epsilon^{-5/3} r_f \xi^{-5/3}. \tag{3.12}$$

Since $r_f/\epsilon \gg 1$, the second term dominates for a typical ξ. From evaluated I:

$$I = 3\epsilon^{1/3}(\delta^{1/3}\epsilon^{-1/3} - 1) + \epsilon^{-2/3} r_f \cdot \frac{3}{2}\left(1 - \left(\frac{\epsilon}{\delta}\right)^{2/3}\right), \tag{3.13}$$

where the first term is negligible since $\epsilon, \delta \ll r_f$, leaving only the second term in I, yielding

$$I \approx \frac{3r_f}{2}\epsilon^{-2/3}\left(1 - \left(\frac{\epsilon}{\delta}\right)^{2/3}\right). \tag{3.14}$$

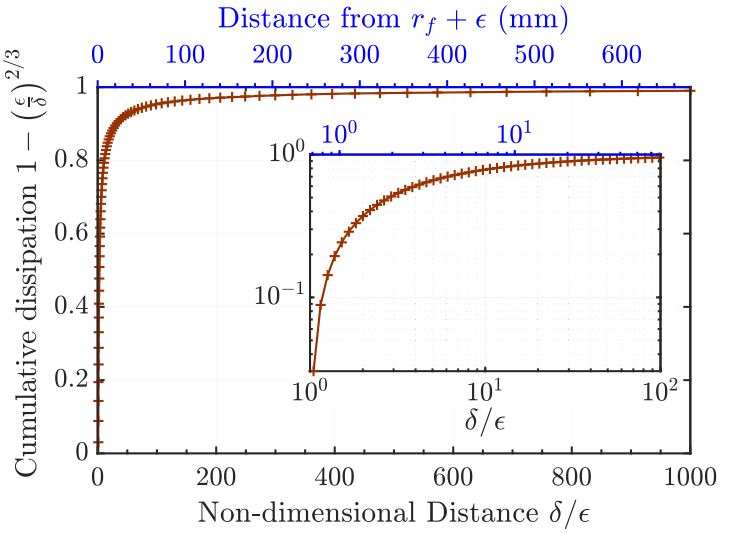

Figure 2. Cumulative viscous dissipation (fraction) versus distance δ/ϵ, equation (3.16). The total amount of dissipation in the fluid in unbonded region accumulates rapidly already close to the bond front. More than 95% of dissipation is accumulated within first 100ϵ of the unbonded region. The inset shows the same data but in log–log scale, with the x-axis zoomed in by factor 10, emphasizing very slow increase in the cumulative viscous dissipation beyond approximately 40ϵ. The two plots are plotted with a shared x-axis, the top axis (in blue) shows distance from the bond in dimensional units. The top (dimensional) x-axis has been computed using $\delta = 1000\epsilon$, and material properties for a standard 300 mm silicon wafer with crystal orientation (100) of $E = 130$ GPa and $T = 775\,\mu$m, unbonded surface adhesion energy $\gamma = 0.1$ J m^{-2}, which results in $A = 0.0064$ m$^{-2/3}$ and $\epsilon = 0.684$ mm (see §3e).

Thus, the dissipation power from equation (3.10) becomes

$$\dot{E}_{\text{diss}} = \frac{18\pi\eta U^2 r_f}{A}(\epsilon^{-2/3} - \delta^{-2/3}). \tag{3.15}$$

The fraction of dissipation up to $r_f + \delta$, relative to an infinite upper limit, is

$$\frac{\dot{E}_{\text{diss},\delta}}{\dot{E}_{\text{diss},\infty}} = \frac{\epsilon^{-2/3} - \delta^{-2/3}}{\epsilon^{-2/3}} = 1 - \left(\frac{\epsilon}{\delta}\right)^{2/3}. \tag{3.16}$$

This non-dimensional fraction, plotted in figure 2, reveals that viscous dissipation is concentrated near the bond front, within a dissipation region of width approximately 100ϵ. This localization, driven by the steep pressure gradient where the gap is smallest, justifies selecting a finite δ, to capture nearly all viscous losses in deriving U (§3e).

However, these relative terms are not fully illustrative of how far downstream from $r_f + \epsilon$ this high-dissipation region is relevant. More importantly, the results are difficult to interpret in practice, given that in industry, most semiconductor bonding processes are done on wafers of diameters 200, 300 mm, and dies spanning approximately 10–50 mm laterally. To address this first, we need to derive a more general expression for U. With a known value of U, we could estimate A, and thus ϵ, from equation (2.15) via

$$2A\epsilon^{5/3} = \Lambda, \quad \text{which is rearranged to } \epsilon = \left(\frac{\Lambda}{2A}\right)^{3/5}, \tag{3.17}$$

where it has been assumed $h \sim \Lambda$. In ambient air, we use the value $\Lambda = 68 \times 10^{-9}$ m.

(e) Solution for U for infinitely long substrates

With $\dot{E}_{\text{diss}}$ re-parameterized by finite radial limits ϵ and δ in equation (3.15), we are now in a position to balance $\dot{E}_{\text{diss}}$ and $\dot{E}_{\text{surf}}$ equation (3.1) to obtain

$$U = \frac{\gamma A}{9\eta(\epsilon^{-2/3} - \delta^{-2/3})}. \tag{3.18}$$

From figure 2, we may make a safe assumption that U is at best marginally affected by any additional viscous dissipation occurring beyond $\delta \gtrsim 1000\epsilon$. With this approximation,

$$\delta^{-2/3} = (1000\epsilon)^{-2/3} = 0.01\epsilon^{-2/3} \quad \text{and} \quad \epsilon^{-2/3} - \delta^{-2/3} = 0.99\epsilon^{-2/3}. \tag{3.19}$$

Since ϵ from equation (3.17) and A from equation (2.19) are known, we can write

$$U = \frac{\gamma(\Lambda/2)^{2/5}}{8.91\eta} \cdot \left(\frac{2187\eta U(1-\nu^2)}{70ET^3}\right)^{1/5}, \tag{3.20}$$

and rearrange for U

$$U = \left(\frac{2187}{70}\right)^{1/4} \frac{\gamma^{5/4}(1-\nu^2)^{1/4}}{(8.91)^{5/4}\eta E^{1/4}\, T^{3/4}} (\Lambda/2)^{1/2}. \tag{3.21}$$

This expression for U recovers the same scalings of the physical and process parameters as Rieutord *et al.* [19] and Poulain *et al.* [25], which are different from Bengtsson *et al.* [16] and Liao *et al.* [24]. As noted in [19], experimentally found dependencies on η by Tong & Gösele [46, fig. 4.23], and on Λ [17] may also compare very well with equation (3.21).

Using typical values available in the literature for the adhesion energy $\gamma = 0.1\,\text{J m}^{-2}$ [17,19,21,27,31,47], and known material properties of a monocrystalline silicon wafer ($\nu = 0.28$, $T = 775\,\mu\text{m}$, $E = 130\,\text{GPa}$) and viscosity of air $\eta = 1.85 \times 10^{-5}\text{Pa s}$, $U \approx 3\,\text{cm s}^{-1}$. This is fairly close to typically reported values (for similarly thick silicon wafers, comparable γ and room-temperature bonding) for example by Sato *et al.* [27], by Stengl *et al.* [48, fig. 3] for room-temperature silicon–silicon bonding, experiments by Larrey *et al.* [23], and modelling results in Liao *et al.* [24] using a hybrid lubrication–molecular description for the dissipation in gas. Typical values of U from equation (3.21) for typically encountered parameter values are shown in figure 3.

Parameter A from equation (2.19) can be solved further by using the final expression for U from equation (3.21), to obtain

$$A = \left(\frac{2187}{70 \cdot 8.91}\right)^{5/12} \left(\frac{\Lambda}{2}\right)^{1/6} \frac{\gamma^{5/12}(1-\nu^2)^{5/12}}{E^{5/12}T^{5/4}}, \tag{3.22}$$

which gives a numerical value for $A \approx 0.0064\,\text{m}^{-2/3}$, and $\epsilon \approx 0.684\,\text{mm}$ in the constant U (or steady-state) scenario. We can also now dimensionalize the distances shown in figure 2 to illustrate that for the typical bonding parameters for a 300 mm silicon wafer, U is dominated by dissipation energy concentrated in approximately the first 20–30 mm region ahead of the bond front. Note that the above derived U allows for the dissipation region between ϵ and δ to move along with the bond front, implying the effective dissipation region can remain of a constant length. Such an ideal situation is rarely realized, as the region between ϵ and δ in the case of a finite substrate will shrink as r_f and $r_f + \epsilon$ move towards the edge.

4. Discussion

(a) Deviation from the steady-state scenario at edge of finite substrate

(i) Towards the edge: in the limit $\epsilon \ll \delta$

As the bond front approaches the wafer edge ($r_f \to R$), the lateral region available for viscous dissipation shrinks. The upper limit in equation (3.10) needs to be replaced by a fixed coordinate

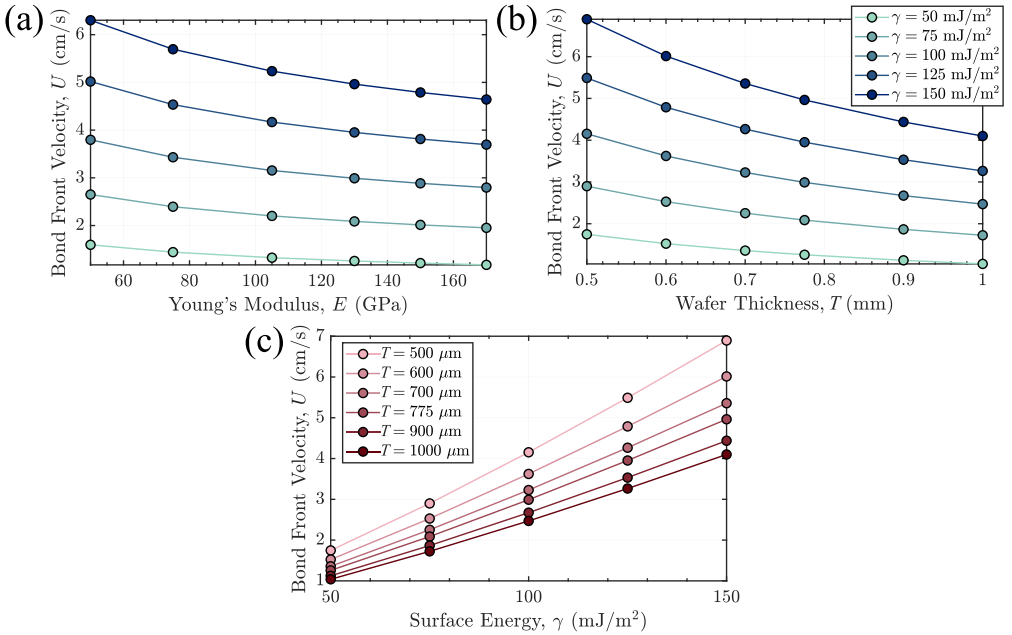

Figure 3. Some values for U based on equation (3.21) are shown for material (Young's modulus E, thickness T) and process-relevant values of surface energy γ. The legend is shared between panels (a) and (b). All results in (a) are calculated using $T = 775\,\mu\text{m}$, while those in panels (b) and (c) with $E = 130\,\text{GPa}$.

R. The integrated $\dot{E}_{\text{diss}}$ from equation (3.15) can then be modified and equated with $\dot{E}_{\text{surf}}$ as

$$2\pi r_f \gamma U = \frac{18\pi\eta U^2 r_f}{A}(\epsilon^{-2/3} - (R - r_f)^{-2/3}), \tag{4.1}$$

which is rearranged for U

$$U = \frac{\gamma A}{9\eta(\epsilon^{-2/3} - (R - r_f)^{-2/3})}, \tag{4.2}$$

while ϵ has the same definition as equation (3.17) and A the same as equation (2.19). Since A is a function of U, so is ϵ via its dependence on A. Note that the numerical value of A from equation (3.22) cannot be used, as it presupposed $\delta = 1000\epsilon$ to obtain equation (3.21). This nonlinear system in equation (4.2) can only be solved numerically to see a growth of U with r_f. The system is solved with `fsolve` in `MATLAB`, and the results are shown in figure 4. For small r_f, the results from equation (4.2) are close to the ideal bond front velocity from equation (3.21). The differences grow with r, and are particularly pronounced in the last few millimetres. The figure does not contain data beyond $r_f \approx 14.95$ cm, as the solver diverges owing to a sharp increase in the solutions sought. We also note that if the distance from the edge is smaller than ϵ, continuum approximation is not valid to define $U(r_f)$. Note that for smaller substrates, while U_∞ equation (3.21) will remain the same, actual $U(r_f)$ may never be close to U_∞. Rather even at the location of bond initiation $r \to 0^+$, higher bond front velocities will occur, since for small substrates, $\delta \sim R$.

(ii) Towards the edge: in the limit $\delta \gtrsim \epsilon$

Much closer to the edge, the approximation in equation (3.14) is invalid, since the extent of dissipation region $\delta \sim \epsilon$. We focus on this region by introducing a small parameter s such that $\delta = \epsilon(1 + s)$ and $s = \frac{\delta - \epsilon}{\epsilon} \ll 1$. We rewrite the integral from equation (3.13):

$$I = \frac{3r_f}{2}(\epsilon^{-2/3} - [\epsilon(1 + s)]^{-2/3}) + 3([\epsilon(1 + s)]^{1/3} - \epsilon^{1/3}), \tag{4.3}$$

https://royalsocietypublishing.org/journal/rspa Proc. R. Soc. A 482: 20260071

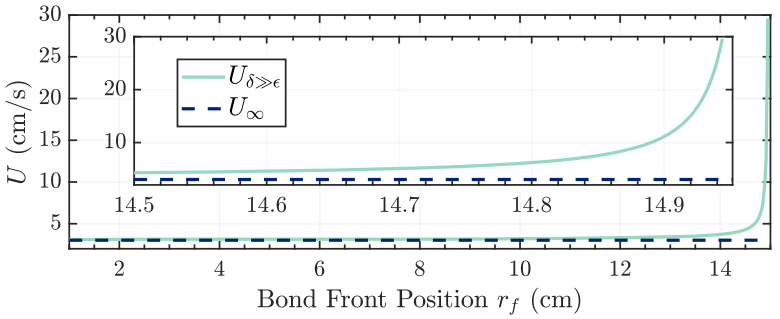

Figure 4. Bond front velocity U vs. position r_f near the wafer edge. The velocity rises as $r_f \to R = 15$ cm, indicating reduced viscous dissipation, compared to the steady state $U_\infty \approx 3$ cm s^{-1} (dashed line, from equation (3.21)). Solid line is computed from equation (4.2). All curves shown were computing using $\epsilon = 0.684\,\mathrm{mm}$ and $\delta = 100\epsilon$. The inset shows a zoomed-in region of the same plot closer to the edge.

and use Taylor expansions for small s,

$$(1+s)^{-2/3} \approx 1 - \frac{2}{3}s + \frac{5}{9}s^2 \quad \text{and} \quad (1+s)^{1/3} \approx 1 + \frac{1}{3}s - \frac{1}{9}s^2. \tag{4.4}$$

We compute the terms in equation (4.3) using the Taylor expansions:

$$\epsilon^{-2/3} - [\epsilon(1+s)]^{-2/3} \approx \epsilon^{-2/3}\left(\frac{2}{3}s - \frac{5}{9}s^2\right) \tag{4.5}$$

and

$$[\epsilon(1+s)]^{1/3} - \epsilon^{1/3} \approx \epsilon^{1/3}\left(\frac{1}{3}s - \frac{1}{9}s^2\right), \tag{4.6}$$

to rewrite I as

$$I \approx r_f \epsilon^{-2/3} s\left(1 - \frac{5}{6}s\right) + \epsilon^{1/3} s\left(1 - \frac{1}{3}s\right). \tag{4.7}$$

The first term dominates on account of both large r_f and small ϵ, such that $I \approx r_f \epsilon^{-5/3}(\delta - \epsilon)$. Thus, a modified $\dot{E}_{\mathrm{diss}}$ is derived. Balancing $\dot{E}_{\mathrm{diss}}$ with an unchanged $\dot{E}_{\mathrm{surf}}$ yields $U \approx \gamma A \epsilon^{5/3}/6\eta(\delta - \epsilon)$, which is simplified further by using the definitions of A and ϵ to obtain

$$U \approx \frac{\gamma \Lambda}{12\eta(\delta - \epsilon)}. \tag{4.8}$$

Since r_f is near the edge, δ is still truncated at the edge as $\delta = R - r_f$, resulting in

$$U \approx \frac{\gamma \Lambda}{12\eta(R - r_f - \epsilon)}. \tag{4.9}$$

This inverse proportionality $U \propto (R - r_f - \epsilon)^{-1}$ will accelerate U at a different rate than that found in equation (4.2). This asymptote in the limit $\delta \gtrsim \epsilon$ is plotted in figure 5 and also compared to U near the edge for the previously considered limit $\delta \gg \epsilon$.

(iii) Implications of the increase in U

The increase of U has also been reported in the literature and was even suggested to result from a reduced dissipation region by [19]. It is understood to be one of the factors responsible for condensing the ambient air close to the edge, which results in entrapped condensation voids—a quality and yield issue in the industry. The mechanism behind condensation voids is the Joule–Thomson effect, and one of the ways condensation voids are being tackled in practice is by using an ambient gas with a negative Joule–Thomson coefficient [49]. It is remarkable that the increase in velocity can be analytically reproduced using this steady-state framework

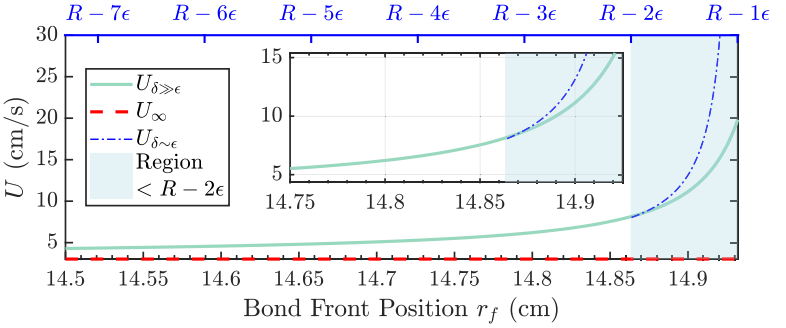

Figure 5. Close to substrate edge, the $\delta \gtrsim \epsilon$ asymptote of U is plotted in dotted–dashed blue curve equation (4.9), alongside the previously shown increase in U (in figure 4 from equation (4.2), in green) and the bond front velocity far from edge U_∞ (from equation (3.21), in red dashed line). The inset shows the cross-over of the two curves: the $\delta \gtrsim \epsilon$ is applicable as the $r_f \to R$ (post the cross-over point), while farther from edge, the green curve is applicable (region to the left-hand side of the cross-over point). The top x-axis shows the distance from the edge in terms of multiples of ϵ. The blue box indicates the region where the representative expression for U changes from equation (4.2) to equation (4.9).

(a lubrication description with no time-dependence), but its accuracy needs to be validated with experiments.

The analytical prediction of increase in $U(r_f \to R)$ may be improved by keeping the unsteady terms in the lubrication description equation (2.1) such that deceleration or acceleration of the bond front will be fully coupled to the gas velocity at r_f. A numerical implementation of such an unsteady lubrication may also incorporate an ad hoc flow condition at $r = R$, where gas from the bond gap meets the atmosphere and is subject to sudden expansion. Further, including kinetic energy of the substrate in the total energy balance (§3b), alongside adhesion energy and viscous dissipation, would also help capture the increased (vertical) speed of the substrate near its edge.

(b) Characteristic velocity and length scales

(i) Representative scale for U in the far-from-edge limit

While the 'steady-state' solution for U (§3e), far from the substrate edge, recovers the scalings found by [19,25] from energetic arguments, it is clear that full non-dimensionalization of the system is not straightforward since the length scales involved span from sub-continuum near the bond front, to the substrate size R where dissipation in the fluid layer can accumulate. To fully generalize the bond front velocity across all regimes, we first use the expression for U from the unsimplified energy balance. Balancing $\dot{E}_{\text{surface}} = \dot{E}_{\text{diss}}$, the exact solution for U is

$$U = \frac{r_f \gamma A}{6\eta \left[\frac{3r_f}{2}(\epsilon^{-2/3} - \delta^{-2/3}) + 3(\delta^{1/3} - \epsilon^{1/3})\right]}, \tag{4.10}$$

which retains all terms in the dissipation integral I and is valid across both steady-state ($\delta \gg \epsilon$) and near-edge ($\delta \approx \epsilon$) regimes. To achieve universality, we intend to define dimensionless groups that capture variation in all material properties, and the shrinking dissipation region. Values of U computed from this full expression are plotted in figure 5 for several values of material parameters that can be readily used in experimental or industrial applications. In comparison to the velocity profiles plotted in figures 4 and 5, the U profiles plotted in figure 6 show a region close to $r = 0$ where the bond front velocity is not constant, but gradually increases to the steady-state values derived §3e. The initially low U for small r in figure 6 occurs owing to domination of viscous dissipation: the area of adhesion at low r is small, whereas the region of viscous dissipation extends until R. Closer to the edge, the steep increase in U resembles the acceleration found in the two approximations $\epsilon \ll \delta$ and $\epsilon \lesssim \delta$.

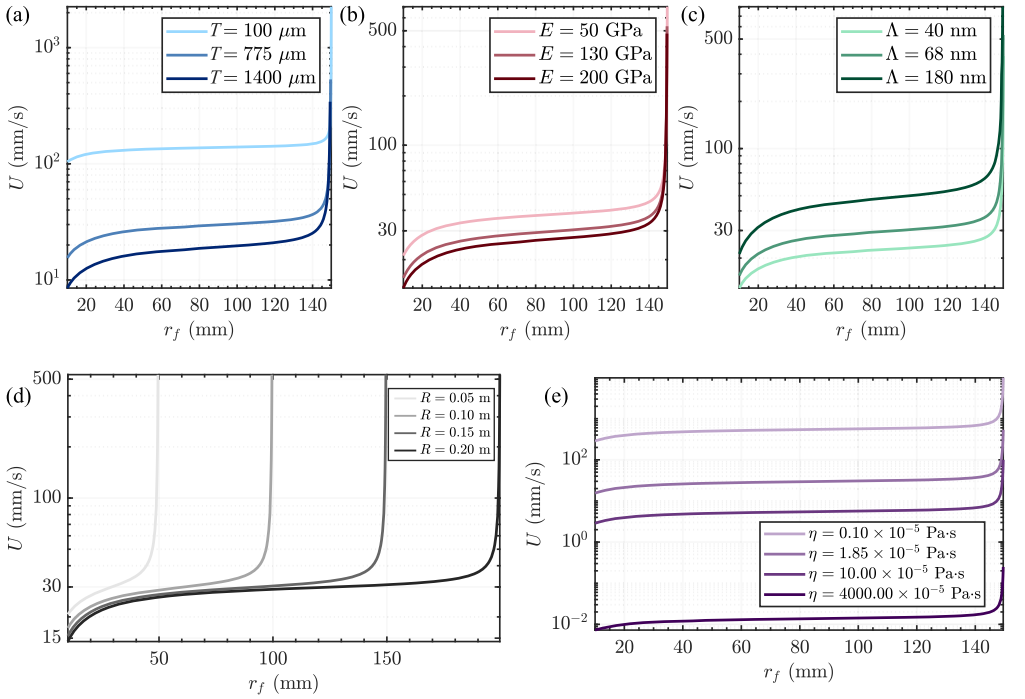

Figure 6. Dimensional values of U computed from equation (4.10) using baseline properties of silicon wafers, unless otherwise stated ($T = 775$ μm, $E = 130$ GPa, $\Lambda = 68$ nm, $R = 150$ mm and air viscosity $\eta = 1.85 \times 10^{-5}$ Pa s). In (a) T is varied; in (b) E is varied; in (c) mean free path of the fluid is varied; in (d) the substrate size is varied while in (e) the fluid viscosity is varied. The general features of the plateau region of U at intermediate r_f, and a steep increase close to the edge are shown in all these panels. The near-edge computations are only valid until $r_f = R - \epsilon$, beyond which the continuum framework cannot describe the dynamics.

Following the steady-state expression for U (equation (3.21)), we can define a characteristic velocity scale,

$$U_{\text{scale}} = \frac{\gamma^{5/4}(1-\nu^2)^{1/4}}{\eta E^{1/4} T^{3/4}} (\Lambda)^{1/2}, \tag{4.11}$$

where all the numerical pre-factors are dropped for simplicity. The results in figure 4.10 are re-plotted in figure 7 with the U rescaled with U_{scale}, and the coordinate rescaled with substrate size R.

The rescaling of velocities in figure 7, U/U_{scale}, brings the velocity-coordinate profiles much closer to each other along the ordinate axis from figure 6 including the variations in T, E, Λ. The abscissa in all the panels were also rescaled by the trivial length scale of substrate size R. Strikingly, a complete collapse of the curves along both abscissa and ordinate is achieved while varying η (figure 7, panel (e)). In panels (a–c), however, some deviations from a unified scaling law curve are dominant in the centre region (bond initiation region) but more importantly in the near-edge region where the velocities rise steeply. The scale U_{scale} over-compensates U in E and T. While the varied curves for different Λ are under-compensated by U_{scale} near the edge. This implies the influence of E and T should shrink close to the edge, while the influence of Λ is relatively underemphasized in the characteristic velocity scale U_{scale}.

Thus we propose another length scale to define the governing dynamics for the acceleration of U observed. This should capture a shrinking influence of E and T with r, or alternatively, an *increasing* influence with *increasing* distance to the edge ($R - r_f$). Since a molecular description is

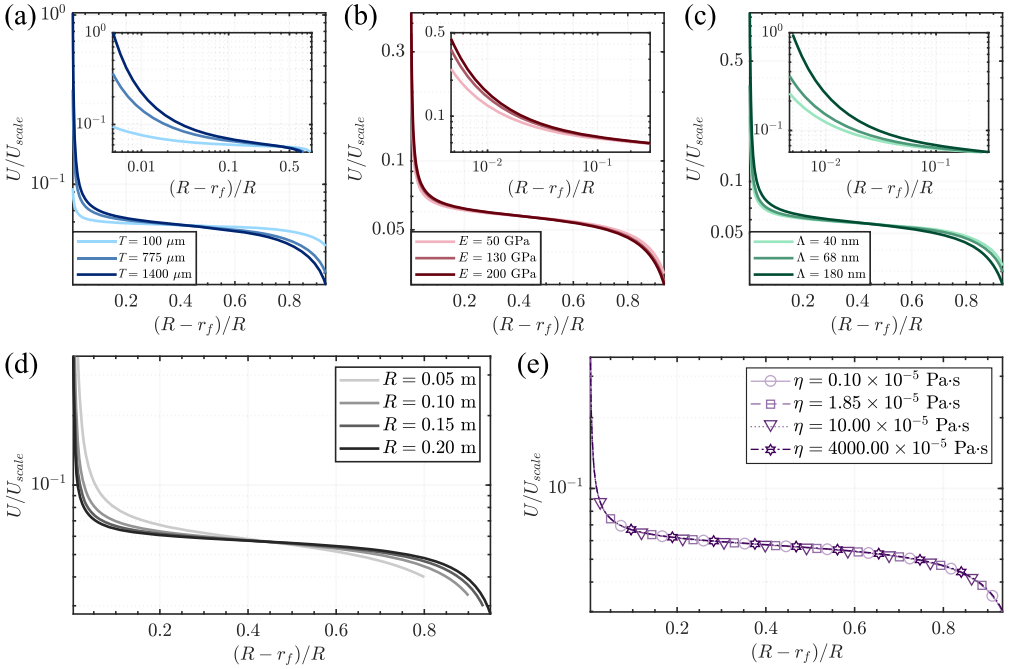

Figure 7. Profiles of U computed from equation (4.10), rescaled by equation (4.11) are plotted with scaled *distance to the substrate edge* $(R - r_f)/R$ for the same parameter sets as shown in figure 6. As the vertical collapse of the curves compared to figure 6 shows, using U_{scale} as the velocity scale indeed captures most of the parametric variation in U. Notably this velocity scale, however, does not collapse the curves near the edges, as shown in insets of panels (a–c). The deviations from a universal curve in panel near $(R - r_f) \to 0$ also indicates the unsuitability of R as the representative length scale. In panel (e), we find a complete and unambiguous collapse of all the curves while varying η.

not contained in the lubrication framework described in the paper, Λ can only enter the definition of this new length scale owing to the role it plays defining the cut-off region at $r_f + \epsilon$.

(ii) Characteristic length scale close to edge

Inspired by the work of Poulain *et al.* [25], who introduced a natural length scale near the adhesion front using the Hamaker constant to balance elasticity against van der Waals' adhesion, scaled by the equilibrium gap height where attractive and repulsive disjoining pressure components equilibrate, we propose an analogous length scale l_c tailored to the near-edge dynamics of our system. In their framework, the length scale emerges from the interplay of intermolecular forces and elastic deformation, providing a characteristic length for the adhesion front. Our approach adapts this, recognizing that the lubrication model employed here lacks a repulsive term, thus necessitating a different balance. We consider the *macroscopic* work of adhesion, represented by the adhesive pressure γ/Λ, balanced by the bending pressure exerted by the wafer's elastic response, approximated as $D\Lambda/l_c^4$. This balance yields a length scale l_c that characterizes the lateral extent of the adhesion front within the continuum regime:

$$l_c = \left(\frac{D\Lambda^2}{\gamma}\right)^{1/4}, \tag{4.12}$$

which is independent of R and shrinking δ, focusing instead on the intrinsic material properties and the molecular scale Λ, making it particularly relevant as the bond front approaches the edge $(r_f \to R)$.

https://royalsocietypublishing.org/journal/rspa Proc. R. Soc. A 482: 20260071

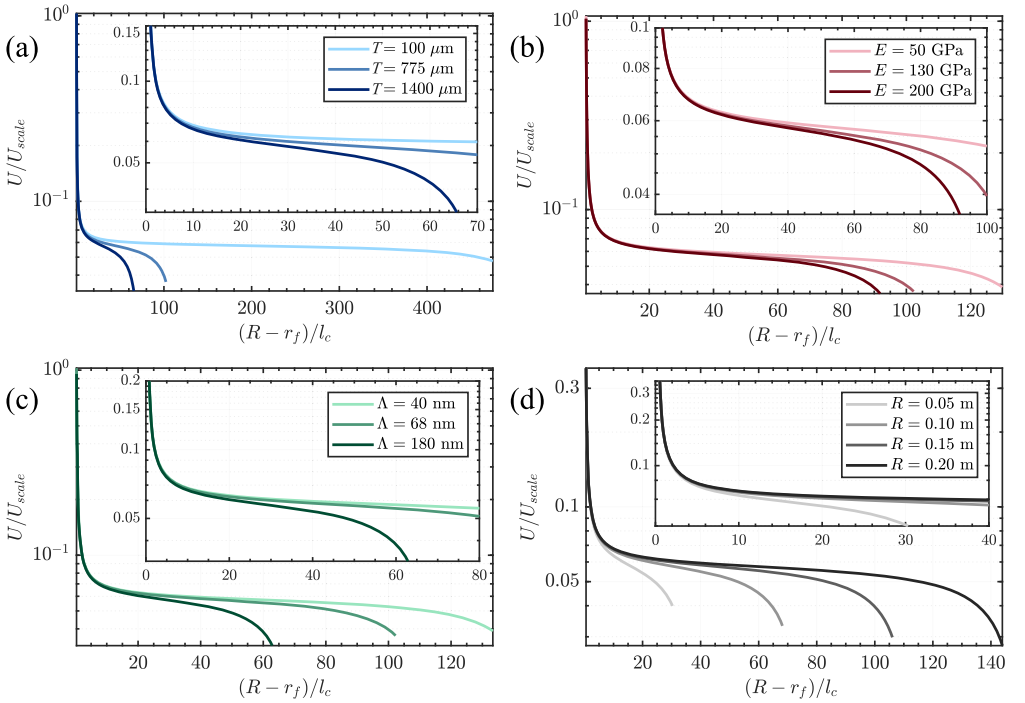

Figure 8. Bond front velocity profiles from figure 7 are plotted against rescaled distance to substrate edge $(R - r_f)/l_c$ using the definition in equation (4.12). These two scales along the respective axes achieve a convincing collapse of the accelerating U close to bond front, with variations shown in T, E, Λ and R. This length scale worsens the collapse in the far-from-edge regime, as it is a representative length scale only close to the bond front. The insets in each panel above show a zoomed-in region of the same plots shown in the main figures.

The efficacy of this length scale is demonstrated in figure 8, where the radial profiles of U/U_{scale}, originally depicted in figure 7, are re-plotted against the rescaled distance $(R - r_f)/l_c$ near the bond front. This normalization results in an excellent collapse of the steeply accelerating U in the near-edge region, where the dissipation length δ becomes comparable to ϵ, and the continuum framework is less applicable. The improved collapse of the curves for variations in T, E, Λ and R underscores the appropriateness of l_c as a characteristic length scale for this regime. Conversely, the collapse deteriorates in the far-from-edge region, which is expected given that l_c is designed to capture the physics of the adhesion front's terminal behaviour. This degradation arises because l_c does not account for the larger-scale geometric effects dominated by R in the far field. The influence of the shrinking δ becomes pronounced only as $r_f + \epsilon$ approaches R, reinforcing the scale's relevance to the near-edge dynamics.

Note that the scale being used in figure 8 loses Λ dependence, and is written (using equations (4.11)–(4.12)) as

$$U_{\text{scale}} \frac{(R - r_f)}{l_c} \sim (R - r_f)(1 - \nu^2)^{1/2} \frac{\gamma^{3/2}}{\eta E^{1/2} T^{3/2}}, \tag{4.13}$$

which for E and T, are rather strikingly the scalings derived by Bengtsson *et al.* [16] (also in §3b) in the absence of viscous dissipation. This signifies a different physical mechanism taking over the front's progression velocity, as any source of viscous dissipation vanishes towards the near-edge limit.

This change in the governing velocity scale implies a transition region between the viscous-dissipation dominated regime and the adhesion-driven regime. In the near-edge regime with

$\delta \sim \epsilon$, equation (4.9) relates to the viscous-dominated scale U_{scale} from equation (4.11) as

$$\frac{U_{\delta\sim\epsilon}}{U_{\text{scale}}} = \frac{1}{12^{3/4}} \frac{l_c}{R - r_f - \epsilon}, \tag{4.14}$$

where the definition of l_c has been used from equation (4.12).

(c) Potential experimental realizations and possible outcomes

The model development throughout this paper assumes an ideal configuration with both wafers 'free-hanging' such that at the bonding interfaces, forces of adhesion act on the compliant substrates and drive the front 'naturally'. This is highly non-trivial to achieve in experiments—this section covers possible set-ups to realize this.

(i) Minimizing the tool influence on natural bond front propagation

Wafers in a tool are typically kept constrained to prevent them from sliding—either with vacuum at several contact points on their backside, or with electrostatic forces [50,51] in the case of high-vacuum tools. In both cases, the severity of tool-interference towards 'natural' bond front progression comes from both the surface on which the wafers are kept constrained, and the magnitude of force that is used to enforce such a constraint.

Thus the first condition to be met is to minimize the contact area between the wafer(s) and the supports holding the wafer during the bond front's progression (henceforth referred to as *wafer table*). This can be achieved by having little contact between wafers' backside and the wafer table—for example, by having a very large number of contact points with small surface area, and a rough surface finish to minimize van der Waals' type adhesion occurring between the wafer backside and the wafer table.

Alternately, the wafers can be kept floating or deflected away from the wafer table by means of a small gas pressure on the backside. In this case, the substrates can be held *weakly* constrained on the wafer table using a weak clamping force (vacuum, electrostatic or mechanical) only along the wafer periphery, which is weak enough that the wafers could be 'peeled-off' from the constraints on a wafer table, when the bond front approaches the edge.

In general, it may be easier to keep at least one of the substrates firmly constrained, and letting the other bond to it. While the physics remains the same, this scenario changes the bonding geometry slightly. Its influence on the bond front velocity is discussed in the next subsection.

(ii) Effect on bond front speed of imposing a (flat) shape on one of the substrates

Another geometrical effect affecting the bonding process in practice, is an imposed shape on one of the substrates. This is the case for both wafer and die bonding, where a device substrate is bonded to a target which can be a carrier (that we call 'bottom' substrate for now) that is kept fixed and calibrated. In such a situation the bonding substrate (or 'top' substrate) remains compliant, while the bottom substrate can be assumed to be rigid. The schematic is shown in figure 9.

When the bottom wafer is imposed as flat and rigid, the gap height is determined solely by the compliant top wafer. The gap size available for the air to squeeze out is halved, and consequently so is the volume flux of the escaping air $Q/2$. The lubrication description and $\partial P/\partial r$ are unchanged, such that the same power law $A(r - r_f)^{5/3}$ describes the top wafer's shape. The functional form of A is also unchanged and $\dot{E}_{\text{diss}}$ is halved on account of the z integrals evaluated between 0 and h (compared to equation (3.4)). The integral definition of U equation (3.8) doubles on account of half the viscous dissipation power. Finally, equating the reduced $\dot{E}_{\text{diss}}$ with an unchanged $\dot{E}_{\text{surf}}$ and solving for U with the same approximation $\delta = 1000\epsilon$ to capture all viscous dissipation, but now modified $\epsilon = (\Lambda/A)^{3/5}$, we obtain a bond front velocity which is $2^{7/4}$(approx. 3.36) times larger than the expression derived in equation (3.21).

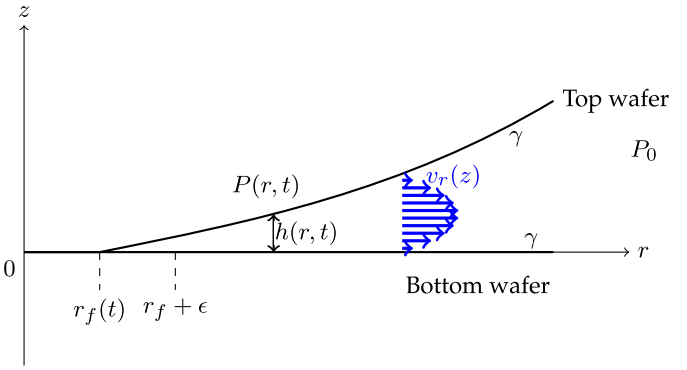

Figure 9. Bonding geometry with a bottom substrate fixed to a rigid support. The gap height $h(r, t)$ is the distance between the top compliant substrate and the flat bottom substrate, with the bond front at $r = r_f(t)$. The position $r = r_f + \epsilon$ marks where $h = \Lambda$ (the mean free path in air for bonding in air), not to scale. Pressure $P(r, t)$ drives air escape against ambient pressure P_0. Blue arrows show the Poiseuille flow profile. Both surface have adhesion energy per unit area of γ.

5. Conclusion

To conclude, this paper describes a lubrication–elasticity treatment of bonding dynamics with the assumptions of steady-state gas flow description, and linear elasticity. Without explicitly accounting for adhesive forces, the two mechanisms that balance the stresses in the fluid and the plate, are the lubrication pressure gradient and the plane-strain bending stresses. While the approximation $U_d \approx U$ used here will not hold throughout the unbonded gap, this approximation is used in the stress balance in the region near r_f to derive a power-law shape (approx. $(r - r_f)^{5/3}$) of the substrate in the region close to the bond front, similar to the result derived and experimentally supported by Rieutord *et al.* [19]. Note that a full fluid–structure interaction may reveal another shape, subject to the imposed boundary and ambient conditions (for instance from matching the lubrication region appropriately with the sub-continuum regime near the bond front, and the ambient outside the confines of the finite substrates).

Next we derived the bond front velocity in this framework by balancing the energy dissipation rates from viscous dissipation and work of adhesion. While the work of adhesion can be a constant for a given pair of surfaces, the viscous dissipation acts over an extended region ahead of the bond front. We show that a careful accounting of the length of this dissipation region is essential to describing the observed velocity that the bond front will eventually exhibit at the gap heights where this continuum framework is valid. By computing the cumulative viscous dissipation, that such a region δ of high dissipation which determines U is concentrated over several distance units ϵ ahead of the bond front, where ϵ is the lateral distance between the point of true gap closure ($h = 0$) and where continuum framework starts to apply (i.e. where h is equivalent to mean free path of the fluid), we show that using this concept of cumulative dissipation, or the lateral region δ/ϵ to determine U, gives the model much more adaptability in determining the variation of U with the bond front's location r_f. In particular, the acceleration of bond front velocity, which is often seen in experiments, can surprisingly be shown here despite starting from steady-state assumptions in the model. Two limits were identified in the near-edge limit, namely when $\delta \gg \epsilon$, and when $\delta \gtrsim \epsilon$. The increase in U with decreasing distance from edge $R - r_f$ was shown in these two limits. The near-edge acceleration couples to the substrate shape h via the dependence of A on U. Thus, an acceleration of the bond front can create a local increase in the steepness of the substrate shape—which (as mentioned in §1) could be a contributing factor to the condensation voids created by isenthalpic expansion (Joule–Thomson effect) of gas volume in the bonding region, typically reported near the edge [49].

Finally, we have tried to describe the unifying velocity and length scales for bonding dynamics discussed in this paper. We showed that a velocity scale U_{scale} is readily identified from the

expression for steady-state bond front velocity, which could capture much of the parametric variation in U computed for several relevant material properties, including substrate thickness and Young's modulus, and the mean free path and viscosity of the fluid. Further, we found that while the trivial length scale in the system, the substrate size R, could approximately capture the radial variation of U in far-field, close to the bond front, this is not a representative length scale. This becomes apparent close to the bond front approaching the edge of a finite substrate, where δ shrinks and molecular scales ought to become more relevant to the bond front dynamics. We introduced a composite length scale (also called natural length scale) l_c similar to the one introduced by Poulain *et al.* [25] to balance the macroscopic work of adhesion with bending stresses, albeit acting over a different vertical distance of Λ (mean free path in our case). It is shown that the lateral length scale non-dimensionalized by l_c achieves an excellent collapse of the radial profiles of U/U_{scale} close to the edge, including the steep acceleration.

As an outlook, the general description of the dynamics may be improved by using an unsteady lubrication equation. The description of substrate dynamics can be more detailed by considering inertial effects, i.e. not just accounting for its potential energy via bending stresses, but also its kinetic energy spent in closing the gap. Further, clamping-like boundary conditions via imposing specific bending moments, and strain-distributions from plate theory, could improve both accuracy and predictive power of the model. If nonlinear elasticity could be included to extend the model to thin plates, it would make the model more useful for instance in die-bonding, in applications involving thin-plate adhesion in flexible electronics, or any industrial process involving coating over air or adhesive materials. This framework finds is natural limitations close to the bond front, where the gap height would go to 8–10 nm in the case of hydrophilic bonding [34], and to the size of surface roughness (sub nanometres) in the case of dry bonding. As a result, this paper focused on the lateral region extending beyond $r_f + \epsilon$ where ϵ denoted the distance from the region with gap width equal to Λ, to the point of true gap closure, such that ϵ delineated the regions between the molecular and continuum description of the gas flow. It is pertinent to note that in hydrophilic bonding, capillary bridges formed by residual monolayers of water near the bond front contribute an additional attraction via capillary condensation. However, at these nanoscale separations, capillary bridges are effective at bonding two surfaces only when the local surface separation falls below the Kelvin length, requiring elastic accommodation of surface roughness asperities [38]. Consequently, both the lateral extent of influence of these capillary/hydrogen-bonding forces and the overall bonding dynamics depend strongly on surface properties: on smoother surfaces (smaller RMS roughness), uninterrupted capillary bridges [52] may form more readily, with their shape at the leading edge determined by surface tension [53]. While their influence on substrate-bending close to the point of *true gap closure* in the region $h \to 0$ (towards trailing edge of the capillary bridges) may be more confined than that in the dry conditions (see $l_{\text{liq, conj}} \sim \mathcal{O}$(tens of microns)) from §2b, the stronger attractive force provided to the substrates by capillary adhesion will strongly affect the bending and bonding dynamics at the leading edge of the capillary bridges. Thus, during bonding, they may effectively contribute to adhesion over a relatively larger effective area, than on rougher surfaces.

Data accessibility. The data are provided in the electronic supplementary material [54].

Declaration of AI use. I have not used AI-assisted technologies in creating this article.

Authors' contributions. U.J.: conceptualization, formal analysis, investigation, methodology, writing—original draft, writing—review and editing.

Conflict of interest declaration. I declare I have no competing interests.

Funding. This work has been enabled in part by the NanoIC pilot line. The acquisition and operation are jointly funded by the Chips Joint Undertaking, through the European Union's Digital Europe (101183266) and Horizon Europe programs (101183277), as well as by the participating states Belgium (Flanders), France, Germany, Finland, Ireland and Romania. For more information, visit nanoic-project.eu.

Acknowledgements. Steven Brems is acknowledged for a careful reading of an earlier version of the manuscript. Paul Grassia's careful and insightful criticism as the editorial board member is gratefully appreciated and helped improve the discussion significantly.

References

1. Beyne E. 2006 3D system integration technologies. In *2006 Int. Symposium on VLSI Technology, Systems, and Applications*, pp. 1–9. (doi:10.1109/VTSA.2006.251113)
2. Iacovo S, Beyne E, Horiguchi N. 2024 Bonding for advanced 3D logic devices. In *2024 8th Int. Workshop on Low Temperature Bonding for 3D Integration (LTB-3D)*, pp. 1–1. IEEE. (doi:10.1109/LTB-3D64053.2024.10774146)
3. Lasky J. 1986 Wafer bonding for silicon-on-insulator technologies. *Appl. Phys. Lett.* **48**, 78–80. (doi:10.1063/1.96768)
4. Wuu SG, Chen HL, Chien HC, Enquist P, Guidash RM, McCarten J. 2022 A review of 3-dimensional wafer level stacked backside illuminated CMOS image sensor process technologies. *IEEE Trans. Electron Devices* **69**, 2766–2778. (doi:10.1109/TED.2022.3152977)
5. Matthias T, Kreindl G, Dragoi V, Wimplinger M, Lindner P. 2011 CMOS image sensor wafer-level packaging. In *2011 12th Int. Conf. on Electronic Packaging Technology and High Density Packaging*, pp. 1–6. IEEE. (doi:10.1109/ICEPT.2011.6067039)
6. Hou S*etal*. 2017 Wafer-level integration of an advanced logic-memory system through the second-generation CoWoS technology. *IEEE Trans. Electron Devices* **64**, 4071–4077. (doi:10.1109/TED.2017.2737644)
7. Kim SW, Fodor F, Heylen N, Iacovo S, De Vos J, Miller A, Beyer G, Beyne E. 2020 Novel Cu/SiCN surface topography control for 1 µm pitch hybrid wafer-to-wafer bonding. In *2020 IEEE 70th Electronic Components and Technology Conference (ECTC)*, pp. 216–222. (doi:10.1109/ECTC32862.2020.00046)
8. Ryan K, Netzband C, Ip N, Hoshino S, Kim H, Gildea A, Tuchman A, LeFevre S, Son I, Aizawa H, Maekawa K. 2023 (Invited) physical analysis and modeling of wafer-to-wafer copper hybrid bonding at sub-micron pitches. *ECS Meeting Abstracts* **MA2023-02**, 1179 (doi:10.1149/MA2023-02171179mtgabs)
9. Plach T, Alexeev A, Flötgen C, Koller L, Dragoi V, Uhrmann T. 2024 Wafer-to-wafer bonding for advanced manufacturing nodes. In *2024 8th International Workshop on Low Temperature Bonding for 3D Integration (LTB-3D)*, pp. 1–1. (doi:10.1109/LTB-3D64053.2024.10772720)
10. Muller P, Bauer O, Raynaud N, Schmidt T. 2024 All-rounder hybrid bond-cluster for wafer to wafer and CO/SEQ die to wafer, room temperature assemblies. In *2024 8th International Workshop on Low Temperature Bonding for 3D Integration (LTB-3D)*, pp. 1–1. (doi:10.1109/LTB-3D64053.2024.10774111)
11. Obreimoff JW, Kapitza PL. 1930 The splitting strength of mica. *Proc. R. Soc. Lond. A* **127**, 290–297. (doi:10.1098/rspa.1930.0058)
12. Strutt RJ. 1936 A study of glass surfaces in optical contact. *Proc. R. Soc. Lond. A* **156**, 326–349. (doi:10.1098/rspa.1936.0151)
13. Yu H, Suo Z. 1998 A model of wafer bonding by elastic accommodation. *J. Mech. Phys. Solids* **46**, 829–844. (doi:10.1016/S0022-5096(97)00100-2)
14. Turner KT, Spearing S. 2002 Modeling of direct wafer bonding: effect of wafer bow and etch patterns. *J. Appl. Phys.* **92**, 7658–7666. (doi:10.1063/1.1521792)
15. Turner K, Spearing S. 2006 Mechanics of direct wafer bonding. *Proc. R. Soc. A* **462**, 171–188. (doi:10.1098/rspa.2005.1571)
16. Bengtsson S, Ljungberg K, Vedde J. 1996 The influence of wafer dimensions on the contact wave velocity in silicon wafer bonding. *Appl. Phys. Lett.* **69**, 3381–3383. (doi:10.1063/1.117266)
17. Gösele U, Hopfe S, Li S, Mack S, Martini T, Reiche M, Schmidt E, Stenzel H, Tong Q. 1995 What determines the lateral bonding speed in silicon wafer bonding? *Appl. Phys. Lett.* **67**, 863–865. (doi:10.1063/1.115530)
18. Tong QY, Gösele U. 1995 Thickness considerations in direct silicon wafer bonding. *J. Electrochem. Soc.* **142**, 3975–3979. (doi:10.1149/1.2048444)
19. Rieutord F, Bataillou B, Moriceau H. 2005 Dynamics of a bonding front. *Phys. Rev. Lett.* **94**, 236101. (doi:10.1103/PhysRevLett.94.236101)
20. Navarro E, Bréchet Y, Moreau R, Pardoen T, Raskin JP, Barthelemy A, Radu I. 2013 Direct silicon bonding dynamics: a coupled fluid/structure analysis. *Appl. Phys. Lett.* **103**, 034104. (doi:10.1063/1.4813312)
21. Navarro E. 2014 Direct wafer bonding dynamics. PhD thesis, Université de Grenoble.
22. Radisson D. 2014 Direct bonding of patterned surfaces. PhD thesis, Université de Grenoble.

23. Larrey V, Mauguen G, Fournel F, Radisson D, Rieutord F, Morales C, Bridoux C, Moriceau H. 2016 Adhesion energy and bonding wave velocity measurements. *ECS Trans.* **75**, 145–152. (doi:10.1149/07509.0145ecst)
24. Liao G, Shi Y, Shi T, Nie L. 2010 Dynamics of contact wave in silicon wafer direct bonding. *IEEE Trans. Adv. Packag.* **33**, 348–352. (doi:10.1109/TADVP.2009.2037730)
25. Poulain S, Carlson A, Mandre S, Mahadevan L. 2022 Elastohydrodynamics of contact in adherent sheets. *J. Fluid Mech.* **947**, A16. (doi:10.1017/jfm.2022.553)
26. Carlson A, Mahadevan L. 2016 Similarity and singularity in adhesive elastohydrodynamic touchdown. *Phys. Fluids* **28**, 011702. (doi:10.1063/1.4938115)
27. Sato R, Nagata A, Kitagawa H, Ogata R, Myalitsin A, Inoue F. 2025 Factors determining bond wave speed in wafer bonding. *Jpn J. Appl. Phys.* **64**, 03SP55. (doi:10.35848/1347-4065/adbafc)
28. Elliott JR, Lira CT. 2012 *Introductory chemical engineering thermodynamics*, 2nd edn. Upper Saddle River, NJ: Prentice Hall.
29. Batchelor G. 2000 *An introduction to fluid dynamics*. Cambridge Mathematical Library. Cambridge, UK: Cambridge University Press.
30. Jennings S. 1988 The mean free path in air. *J. Aerosol Sci* **19**, 159–166. (doi:10.1016/0021-8502(88)90219-4)
31. Gui C, Elwenspoek M, Tas N, Gardeniers JG. 1999 The effect of surface roughness on direct wafer bonding. *J. Appl. Phys.* **85**, 7448–7454. (doi:10.1063/1.369377)
32. Inoue F*etal*. 2019 Influence of composition of SiCN as interfacial layer on plasma activated direct bonding. *ECS J. Solid State Sci. Technol.* **8**, P346–P350. (doi:10.1149/2.0241906jss)
33. Spierings G, Haisma J, Michelsen T. 1995 Surface-related phenomena in the direct bonding of silicon and fused-silica wafer pairs. *Philips J. Res.* **49**, 47–63. (doi:10.1016/0165-5817(95)82003-5)
34. Moriceau H, Rieutord F, Fournel F, Le Tiec Y, Di Cioccio L, Morales C, Charvet A, Deguet C. 2010 Overview of recent direct wafer bonding advances and applications. *Adv. Natural Sci.: Nanosci. Nanotechnol.* **1**, 043004. (doi:10.1088/2043-6262/1/4/043004)
35. Landau LD, Pitaevskii L, Kosevich AM, Lifshitz EM. 1986 *Theory of elasticity*, **7**. 3rd edn, vol. Amsterdam, The Netherland: Elsevier.
36. Kaplan W. 2003 *Advanced calculus*. Addison-Wesley Higher Mathematics Series. Reading, MA (Wokingham, UK): Addison-Wesley.
37. Israelachvili J. 2010 *Intermolecular and surface forces*, 3rd edn. Intermolecular and Surface Forces. New York (Orlando, FL/London/San Diego, CA): Academic Press.
38. Persson B, Mate CM. 2024 Role of humidity and surface roughness on direct wafer bonding. *Eur. Phys. J. B* **97**, 46. (doi:10.1140/epjb/s10051-024-00680-w)
39. Valmacco V, Elzbieciak-Wodka M, Besnard C, Maroni P, Trefalt G, Borkovec M. 2016 Dispersion forces acting between silica particles across water: influence of nanoscale roughness. *Nanoscale Horiz.* **1**, 325–330. (doi:10.1039/C6NH00070C)
40. Moffatt H. 2019 Singularities in fluid mechanics. *Phys. Rev. Fluids* **4**, 110502. (doi:10.1103/PhysRevFluids.4.110502)
41. Morgan J, Cox S. 2024 Effects of liquid fraction and contact angle on structure and coarsening in two-dimensional foams. *J. Fluid Mech.* **999**, A10. (doi:10.1017/jfm.2024.756)
42. Ip N, Nagata A, Kohama N, Wada N, Motoda K. 2020 Investigation of post-bond distortion in direct wafer bonding. *ECS Trans.* **98**, 47–52. (doi:10.1149/09804.0047ecst)
43. Netzband C, Ryan K, Mimura Y, Ilseok S, Aizawa H, Ip N, Chen X, Fukushima H, Tan S. 2023 0.5 µm pitch next generation hybrid bonding with high alignment accuracy for 3D integration. In *2023 IEEE 73rd Electronic Components and Technology Conference (ECTC)*, pp. 1100–1104. IEEE. (doi:10.1109/ECTC51909.2023.00188)
44. Dragoi V, Rebhan B, Pabo E. 2020 Direct wafer bonding methods: A practical process selection guide. *ECS Trans.* **98**, 33–46. (doi:10.1149/MA2020-02221651mtgabs)
45. Dragoi V, Lindner PF. 2020 Wafer-bonding equipment. In *Handbook of Silicon Based MEMS Materials and Technologies*, pp. 648–663. Elsevier. (doi:10.1016/B978-0-323-29965-7.00034-8)
46. Tong QY, Gösele U. 1999 *Semiconductor wafer bonding: science and technology*. New York: John Wiley & Sons.
47. Dragoi V, Farrens S, Lindner P, Weixlberger J. 2004 Low temperature wafer bonding for microsystems applications. In *2004 Int. Semiconductor Conference. CAS 2004 Proceedings (IEEE Cat. No. 04TH8748)*, vol. 1. IEEE. (doi:10.1109/SMICND.2004.1402839)
48. Stengl R, Tan T, Gösele U. 1989 A model for the silicon wafer bonding process. *Jpn J. Appl. Phys.* **28**, 1735. (doi:10.1143/JJAP.28.1735)

49. Fournel F, Larrey V, Morales C, Michaud LG. 2023 Edge bonding voids management using humid helium bonding atmosphere. *ECS Trans.* **112**, 15–22. (doi:10.1149/11203.0015ecst)
50. 2017 *Design of an active wafer clamp for wafer machines*. PhD thesis, Technische Universiteit Eindhoven.
51. Veeraraghavan S, Sohn J, Turner KT. 2007 Techniques to measure force uniformity of electrostatic chucks for EUV mask clamping. In *Photomask Technology 2007*, vol. 6730. p. 67305G. International Society for Optics and Photonics SPIE. (doi:10.1117/12.746843)
52. Persson BNJ. 2008 Capillary adhesion between elastic solids with randomly rough surfaces. *J. Phys.: Condens. Matter* **20**, 315007. (doi:10.1088/0953-8984/20/31/315007)
53. Kim S, Kim D, Kim J, An S, Jhe W. 2018 Direct evidence for curvature-dependent surface tension in capillary condensation: Kelvin equation at molecular scale. *Phys. Rev. X* **8**, 041046. (doi:10.1103/PhysRevX.8.041046)
54. Jain U. 2026 Bond front velocity in lubrication-mediated bonding of flexible substrates. Figshare. (doi:10.6084/m9.figshare.c.8452075)